JGR Atmospheres

RESEARCH ARTICLE
10.1029/2024JD043303

Special Collection:
Coupling wildfire behavior and atmospheric dynamics: The California Fire Dynamics Experiment (CalFiDE)

Wildfire Smoke Shading Observations: Impacts on Boundary Layer Mixing and Thermally Driven Smoke Transport

Brian J. Carroll[1,2], Edward Strobach[1,2,3], Sunil Baidar[2], Maxwell W. Holloway[1,2], Brandi McCarty[1,2], Richard Marchbanks[1,2], and W. Alan Brewer[2]

[1]Cooperative Institute for Research in Environmental Sciences, University of Colorado Boulder, Boulder, CO, USA, [2]Chemical Sciences Laboratory, National Oceanic and Atmospheric Administration, Boulder, CO, USA, [3]Atmospheric and Oceanic Sciences Department, University of Maryland, College Park, MD, USA

Abstract Smoke shading from wildfire smoke cools the surface and atmosphere below the smoke by absorbing and scattering sunlight. This has the potential to create meteorological feedback and large air quality impacts, but observations of smoke shading and induced local flows are rare. Mobile truck-based Doppler lidar observations during the California Fire Dynamics Experiment (CalFiDE) in August and September 2022 provide a novel data set of smoke shading events. The truck-based lidar conducted measurements of horizontal and vertical winds while underway, along with qualitative smoke backscatter, allowing a study of boundary layer (BL) dynamics in and out of the smoke shaded areas. An in situ temperature sensor on the truck recorded air temperature. Smoke shaded versus clear-sky temperature differences of up to 8°C were observed over 12 km along a valley floor in complex terrain. Using vertical velocity variance as a measure of turbulent mixing, smoke shading reduced BL mixing by up to two orders of magnitude, preventing the development of an afternoon convective BL in some cases. Temperature gradients also resulted in thermally driven flows wherein the cold smoky air mass undercut warmer ambient air. One density current case was observed with a strong opposing flow resulting in a convergent updraft and shear-induced vortices atop the smoke-filled density current. In another case, the flow was impeded by complex terrain resulting in a slower-moving smoke front and a temperature gradient that lagged behind the front.

Plain Language Summary Visibly thick wildfire smoke blocks sunlight from reaching the ground. This results in cooler temperatures in smoke-shaded areas. These cooler temperatures contribute to trapping smoke from active or smoldering fires especially in valleys. Smoke shading impacts on local weather patterns have only been observed a few times in past research, and this study uses state-of-the-art measurements from a moving truck to provide new insights. The smoke shading modified the lowest layers of the atmosphere and caused flow patterns that transported the dangerously high concentrations of smoke away from the fire.

Key Points:

- Wildfire smoke shading caused reduced daytime boundary layer (BL) turbulence with substantial heterogeneity on kilometer scales
- Smoke shading causes temperature gradients that can lead to localized flows that are modified by terrain and other forcing mechanisms
- Profiling from moving platforms provides new insights into BL dynamics especially in complex terrain

Supporting Information:

Supporting Information may be found in the online version of this article.

Correspondence to:
B. J. Carroll,
brian.carroll-1@colorado.edu

Citation:
Carroll, B. J., Strobach, E., Baidar, S., Holloway, M. W., McCarty, B., Marchbanks, R., & Brewer, W. A. (2025). Wildfire smoke shading observations: Impacts on boundary layer mixing and thermally driven smoke transport. *Journal of Geophysical Research: Atmospheres*, *130*, e2024JD043303. https://doi.org/10.1029/2024JD043303

Received 31 DEC 2024
Accepted 12 JUN 2025

Author Contributions:
Conceptualization: Brian J. Carroll, Sunil Baidar, Maxwell W. Holloway, Brandi McCarty, Richard Marchbanks
Data curation: Brian J. Carroll, W. Alan Brewer

1. Introduction

Wildfire smoke is a major health hazard due to the potential for high concentrations of $PM_{2.5}$ and ozone. Transported smoke can cause severe air quality thousands of kilometers away, and in stagnant conditions, the areas near a fire can become the most polluted areas on the planet (Bernstein et al., 2021; Bowman et al., 2009; Jaffe & Wigder, 2012; Kochanski et al., 2019; Langford et al., 2023). Local and transported wildfire smoke are offsetting the benefits of $PM_{2.5}$ regulations in the northwest US (McClure & Jaffe, 2018; O'Dell et al., 2019). Along with these health impacts, smoke particles can scatter and absorb a substantial amount of solar radiation. This effect is known as smoke shading, and it can modify meso- and smaller-scale meteorology by generating temperature gradients between shaded and clear-sky areas.

By the early 1990s, it was recognized that smoke shading with sufficient optical depth can cause substantial surface cooling and can trigger a positive feedback mechanism wherein a temperature inversion traps more smoke at the surface and persists in smoke-filled valleys for days (Robock, 1988, 1991; Segal et al., 1989). It was hypothesized and modeled that such localized cooling could induce mesoscale circulations such as modified drainage flows or sea breezes (Garratt et al., 1990) though Segal and Arritt (1992) noted the lack of observations proving such induced circulations. Observational studies have since shown cooling both locally and after long-range transport impacts on air temperature aloft, and anomalous pressure increases in smoke-shaded areas (Hobbs

Formal analysis: Brian J. Carroll, Edward Strobach
Investigation: Brian J. Carroll, Sunil Baidar
Methodology: Brian J. Carroll, Sunil Baidar
Resources: Maxwell W. Holloway
Supervision: W. Alan Brewer
Visualization: Brian J. Carroll, Edward Strobach, W. Alan Brewer
Writing – original draft: Brian J. Carroll
Writing – review & editing: Brian J. Carroll, Edward Strobach, Sunil Baidar

et al., 1997; Pahlow et al., 2005; Stone et al., 2011; Youn et al., 2011). Pan and Faloona (2022) used monitoring sites in California's Central Valley over 5 years to calculate reduced surface buoyancy flux (−30%), downwelling shortwave radiation (−54 W m^{-2}), and planetary boundary layer (BL) height (−80 m, 15%) during periods with wildfire smoke. However, due to the transient nature of wildfires and smoke shading and challenges with measuring in the complex remote terrain where large fires often occur, no detailed studies of smoke-induced mesoscale flows existed in the literature until Lareau and Clements (2015). Lareau and Clements (2015) showed multiple cases of propagating smoke fronts with a density current structure using Doppler lidar data and cameras. These featured sharp gradients in smoke concentration coinciding with a strong thermal gradient induced by smoke shading and propagated according to standard density current theory in some cases. Other observational studies featuring Doppler lidar measurements of wildfire smoke have focused on wildfire plume turbulent properties and injection height using Doppler lidar and other instrumentation (Carroll et al., 2024; Clements et al., 2018; Lareau & Clements, 2017; Strobach et al., 2023, 2024). However, observations of smoke shading and mesoscale flows like those by Lareau and Clements (2015) are still lacking in the literature.

The impacts of smoke shading are challenging to model despite the important ramifications for air quality and fire management. Along with the computational expense of radiative transfer, the wide range of smoke particle absorption and scattering properties adds variable complexity to smoke radiative properties dependent on fuel and fire conditions (Bernstein et al., 2021; Bian et al., 2020; Colbeck et al., 1997; Goodrick et al., 2012; Noyes & Kahn, 2024). Current numerical weather prediction models generally do not account for these aerosol radiative effects or other coupled fire-atmosphere interactions. Kochanski et al. (2019) recently presented the first modeling study focused on small-scale processes associated with fire-atmosphere interactions, including smoke shading, using a coupled fire-atmosphere model integrated with a chemical model. They confirmed localized surface cooling effects and the positive feedback mechanism of a strengthening inversion continuing to trap more smoke. These inversions inhibited BL growth and reduced surface winds.

This manuscript presents observations of smoke shading dynamics using mobile Doppler lidar, including smoke-filled valleys, smoke-induced thermally driven flows (density currents), and impacts of smoke shading on BL turbulent mixing. Section 2 covers instrument details, Section 3 provides relevant fire information, Section 4 presents a case study of smoke-filled valley impacts on BL properties, and Section 5 has two case studies of smoke fronts with thermally driven flows.

2. California Fire Dynamics Experiment (CalFiDE) and Instrumentation

The CalFiDE campaign featured mobile platforms with a diverse suite of instrumentation to study wildfire behavior coupled to atmospheric dynamics as well as smoke plume emissions and chemistry from 28 August to 25 September 2022 (Carroll et al., 2024; see also Noyes & Kahn, 2024; Strobach et al., 2024). The mobile airborne and ground-based platforms were typically deployed in coordination at a given fire to make complementary measurements but occasionally a platform operated independently for logistical reasons (e.g., at the Mountain fire examined in this study). Only 3 days had observations of sharp gradients in smoke shading suitable for this study.

2.1. The Pick-Up Based Mobile Atmospheric Sounder (PUMAS)

PUMAS is a unique truck-based asset designed and built at the NOAA Chemical Sciences Laboratory to enable three-dimensional wind profiling above the vehicle while underway. It was deployed for the entire duration of CalFiDE. The primary instrument is a Doppler lidar system (Schroeder et al., 2020) featuring two channels: one staring vertically to measure the vertical wind (w) at a high repetition rate and one scanning 15° off zenith to retrieve horizontal winds. Active motion stabilization of the lidar transceiver helps remove platform motion and retrieve true atmospheric winds (Carroll et al., 2024).

The lidar vertical resolution was 62 m for the vertical staring channel and 60 m for the scanning channel with a minimum range of 120 m. The lidar can operate within a range of temporal resolutions and scanning rates chosen depending on the atmospheric conditions and scientific goals. Here, the data shown have a vertical measurement (profile of w) every 2 s and a profile of horizontal wind vectors every 18 s. These periods translate to along-track resolutions that vary based on the movement of the truck. For this study, along-track resolution of the PUMAS lidar data was generally finer than 55 and 500 m for w profiles and wind profiles, respectively.

The lidar operates at 1.54 μm and thus the backscattered signal mainly comes from aerosols (i.e., not air molecules). This is well-suited for measurements in the BL where aerosols are most abundant and has the added advantage of being particularly sensitive to smoke. The power of the returning signal has a range dependence that can be characterized and removed yielding a profile of range-corrected intensity (RCI, e.g., Bonin & Brewer, 2017). Assuming fairly uniform aerosol bulk scattering properties within a given profile, RCI provides information on the vertical distribution of aerosols. This cannot be converted to a quantitative aerosol backscatter or concentration without reference measurements and significant assumptions. Regarding the comparability of temporally distant RCI profiles, PUMAS splits power between the vertical and scanning channels and that power ratio drifted during CalFiDE. This does not diminish the data quality, but it does disallow quantitative comparison of backscatter profiles that are temporally distant or when there is a clear sudden shift in the channel power ratio. However, RCI changes over shorter timescales are informative, and values at different altitudes within a given profile can always be compared.

The w measurements from PUMAS can be used to retrieve profiles of w variance ($\overline{w'^2}$), a common measure of mixing and proxy for turbulent kinetic energy (Bonin et al., 2017). This retrieval is commonly performed with stationary Doppler lidars using the evenly spaced timeseries data and an assumption of constant (or averaged) horizontal wind (Lenschow et al., 2000). Since PUMAS is mobile, the amount of atmosphere passing horizontally through the sampling volume (i.e., fetch) can vary greatly with each measurement. This complicates identification of the inertial subrange in the traditional $\overline{w'^2}$ retrieval methodology, so the PUMAS w data were converted from an evenly spaced timeseries to an evenly spaced spatial series for each height by averaging into bins of platform-relative fetch equal to the range gate length. The evenly spaced spatial series was used to retrieve the $\overline{w'^2}$.

PUMAS also made in situ temperature measurements on a forward-mounted boom 3 m above the ground (T_{3m}) and had an all-sky camera during CalFiDE. The temperature sensor was mounted forward so that it measured air unaffected by the truck while underway, but heat rising from the engine caused T_{3m} biases while stationary so those data have been removed.

2.2. Ground Sites

Long-term in situ monitoring stations can also provide valuable measurements to study smoke shading, adding information on temporal evolution at certain locations without the spatial coverage that PUMAS provided. This study uses three types of monitoring sites: Remote Automatic Weather Stations (RAWS), Automated Surface Observing Systems (ASOS), and a $PM_{2.5}$ measurement site. RAWS and ASOS sites provide a broad range of standard meteorological measurements. The RAWS sites used here are Merlin (MLFO3, 42.500°, −123.369°, elevation 349 m) and Mt. Shasta (MSAC1, 41.315°, −122.317°, elevation 1,089 m). The ASOS site is located at Grants Pass Airport (K3S8, 42.510°, −123.387°, elevation 343 m). The $PM_{2.5}$ site is operated by the Oregon Dept. of Environmental Quality, located in Grants Pass (42.434°, −123.358°, elevation 292 m).

3. The Fires

Observations used for this study are from two different fires observed on cloud-free days so that impacts from clouds are not conflated with smoke shading. Observations were only considered between 5 hr after sunrise and 1.5 hr before sunset (11:40–18:15 local time), when we would expect a well-developed convective BL in the afternoon under clear-sky summer conditions (e.g., Bonin et al., 2018). Local time was UTC—7 hr.

3.1. The Rum Creek Fire

The Rum Creek fire started on 17 August 2022 in complex mountainous terrain just west of Merlin, Oregon (42.641°N, −123.628°W). The fire burned 12,000 acres before the CalFiDE observation dates of 30 August and 1 September with an additional 3,000 total acres burned over the observation days. Along with smoldering from the previously burned area, this created very smoky conditions and the development of smoke-filled valleys overnight. The fire perimeter from 1 September is shown in Figure 1a with terrain shading of the surrounding region and the PUMAS drive route. The fire burned the Rogue River valley and surrounding mountaintops near the town of Merlin, Oregon.

Figure 1b shows visible satellite imagery from that afternoon with the PUMAS drive route at times within completely opaque smoke and at other times in fairly clear-sky areas. The southwest and northwest endpoints of

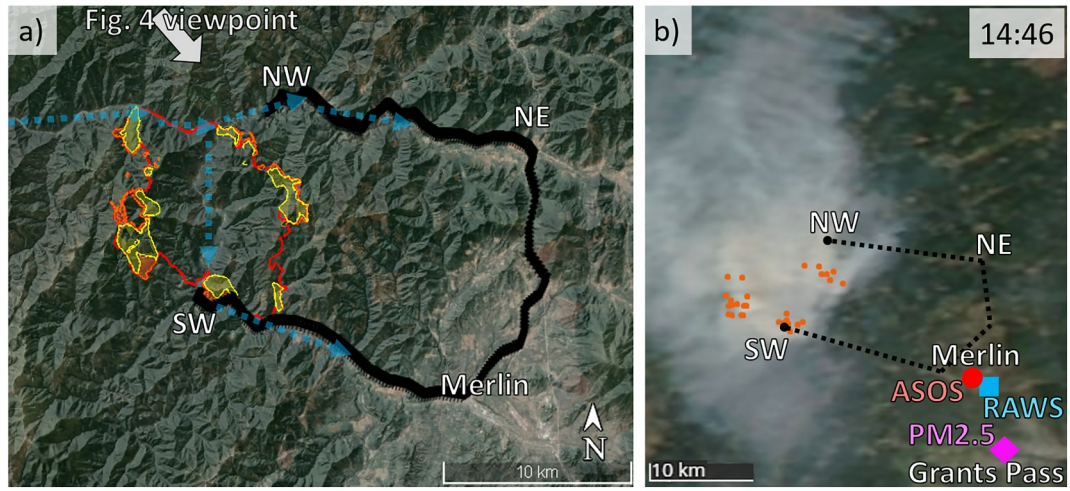

Figure 1. (a) Map of the Rum Creek fire area with terrain shading superimposed on satellite visible imagery. The 1 September fire perimeter is in red with yellow and orange indicating intense heat (National Interagency Fire Center, 2023). The black track is the PUMAS drive track that was repeated continuously on observation days, passing through the town of Merlin, Oregon. The blue arrows indicate a sea breeze path up the river valley. (b) NASA Aqua MODIS imagery and hotspots (orange dots) from the 1 September 14:46 local time overpass. Black lines are the approximate PUMAS drive route shown in panel (a). Automated Surface Observing Systems, Remote Automatic Weather Stations, and $PM_{2.5}$ surface monitor sites are marked in panel (b).

the route, marked SW and NW, were in smoke-filled valleys very near the fire that rarely saw clearer conditions on the observation days. The eastern portion of the route was intermittently clear and smoky due to variable transport and build-up. PUMAS took observations from 10:00 to 19:00 local time on 30 August and 12:00 to 21:00 on 1 September.

The observation period was characterized by high pressure with a weak trough aligned parallel to the coastline present at some times but no frontal passages (https://www.wpc.ncep.noaa.gov/archives/web_pages/sfc/sfc_archive_maps.php?arcdate=09/01/2022&selmap=2022090121).

3.2. The Mountain Fire

The Mountain fire started on 2 September 2022 in complex mountainous terrain northwest of Mt Shasta, California (41.459°N, −122.627°W). The fire grew from 8,896 acres to 11,690 acres on the date of interest for this study, 5 September. The fire perimeter on this date is shown in Figure 2a with important PUMAS observation locations and drive segments A–E noted for context. The period was characterized by high pressure in the Pacific Northwest and east of the Sierra Mountains and low pressure in the California Central Valley. Some of the surface analysis maps from 5 September day show a weak stationary front extending from Montana to northern California though surface winds were quite weak in the area (NOAA Weather Prediction Center surface analysis: https://www.wpc.ncep.noaa.gov/archives/web_pages/sfc/sfc_archive_maps.php?arcdate=09/05/2022&selmap=2022090521).

Figures 2b and 2c show the change in conditions from the morning with smoke-filled valleys to the west and no distinct plume aloft to the afternoon, which had southwesterly winds aloft directing an elevated smoke plume over the basin to the east. The smoke was optically thick enough to drastically obscure visible imagery of the surface—a sharp change from the clear-sky conditions east of the fire in the morning. Considering the terrain, drainage flow from the source region should propagate through the valley indicated by white arrows in Figures 2b and 2c where there was indeed a large increase in smoke coverage.

For this case study, only PUMAS was operating at the Mountain fire. Also, the Mountain fire occurred in fairly remote and complex mountainous terrain with insufficient ground-based observing network installations to provide useful insight into this case study. We therefore will only present data from PUMAS.

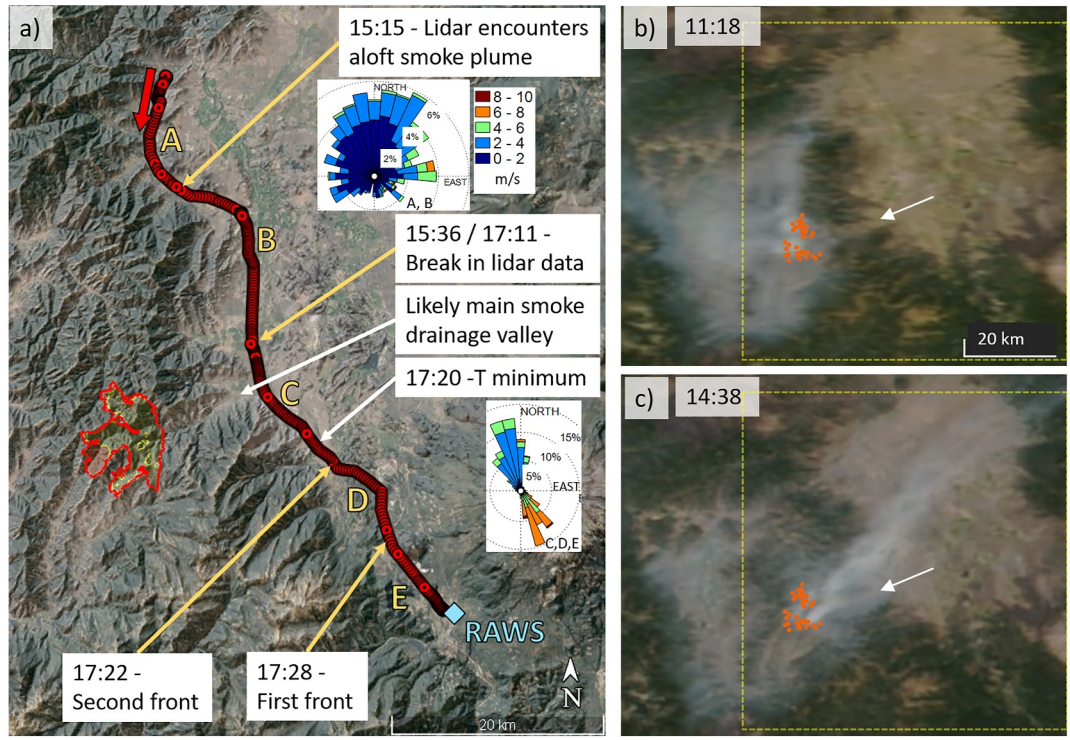

Figure 2. (a) Map of the Mountain fire area with terrain shading. The 5 September fire perimeter is in red on the left (National Interagency Fire Center, 2023). The red/black circles indicate the PUMAS drive track with arrows and text indicating key locations and local times. Yellow arrows and letters segment the track as discussed later. Wind roses are below 600 m AGL and separated for segments A, B, and for C, D, E (presented full-size in Figure S1 in Supporting Information S1). (b, c) Visible imagery from (b) NASA Terra MODIS and (c) Suomi NPP VIIRS with MODIS hotspots in orange. The local time of each overpass is in the upper left. The smoke drainage valley is indicated by the white arrow. The yellow box in panels (b, c) indicates the area shown in panel (a).

4. Smoke Shading at the Rum Creek Fire

In this section, we present the available metrics of smoke amount in the Rum Creek fire region ($PM_{2.5}$, AOD, and PUMAS lidar RCI) and the observed changes in BL temperature and dynamics that accompanied smoke shading.

4.1. Overview of Rum Creek Fire and Smoke on 30 August and 1 September

The closest available $PM_{2.5}$ measurement timeseries (in Grants Pass, Oregon, see Figure 1b) is shown in Figure 3a. The station was 25 km from the fire and 11 km from the nearest PUMAS measurement, so given the complex terrain and spatiotemporal variability of smoke concentrations it can only be used somewhat qualitatively as an example of the nearby $PM_{2.5}$ air quality severity and larger-scale flow timings in conjunction with the nearby RAWS and ASOS sites. Downwelling solar radiation is plotted in Figure 3a reported as a 60-min average from the RAWS site ~7 km north of the $PM_{2.5}$ site. Winds are shown in Figure 3b from the ASOS site 1.9 km northwest of the RAWS site.

30 August, the evening before the first PUMAS observations, had a buildup of $PM_{2.5}$ to severely unhealthy levels (a peak of 335 μg m^{-3}) that persisted overnight. During the following day concentrations were variable but overall decreased likely due in part to transport evidenced by increased wind speeds in the surface station data. There is an apparent diurnal pattern common to the 3 days shown with steady values overnight, variable concentrations during the day, and a sharp spike in $PM_{2.5}$ in the late afternoon. Smoke production is generally expected to peak in the afternoon along with fire activity, but the $PM_{2.5}$ timeseries here clearly indicates the dominance of transport over the diurnal production cycle for this site.

The timing of the late afternoon spike each day was coincident with the appearance of northwesterly winds after stagnation likely pushing accumulated Rum Creek smoke over the measurement sites. The direction, timing, and

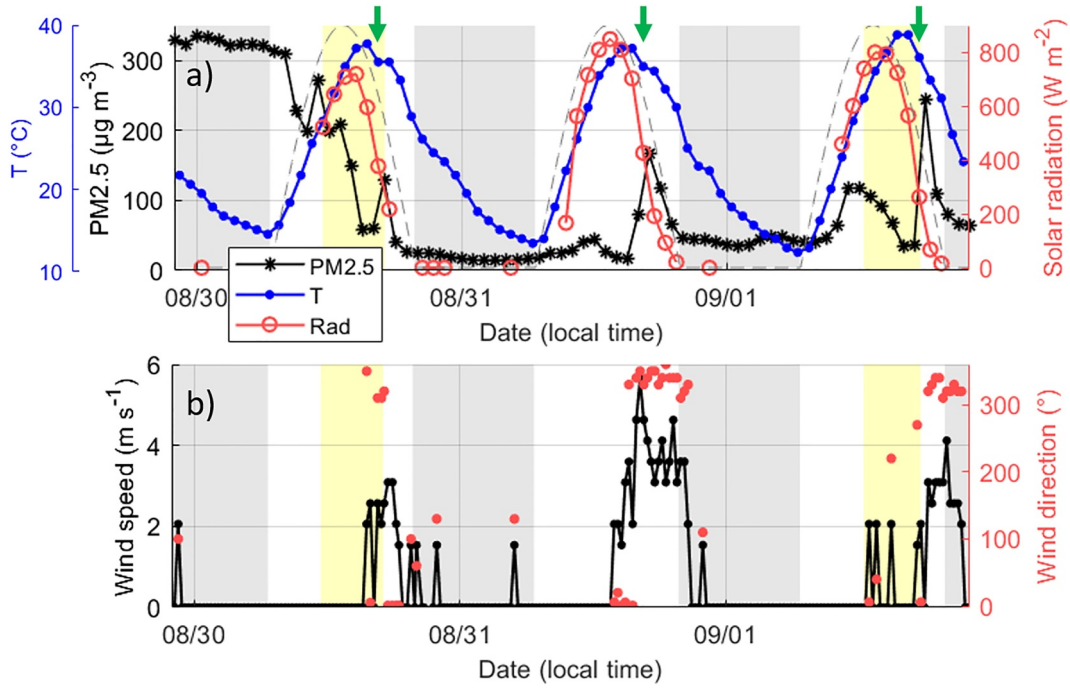

Figure 3. (a) $PM_{2.5}$ from the Grants Pass site and 2 m air temperature and solar radiation from the Merlin Remote Automatic Weather Stations site. Gray dashed line is a cloud-free solar radiation reference line. (b) Wind speed and direction from the Grants Pass Airport Automated Surface Observing Systems site. Gray shading is nighttime, and yellow shading is the PUMAS observation periods. Green arrows indicate temperature drops discussed in the text.

appearance only at low altitudes are consistent with a sea breeze, bringing cleaner air up the Rogue River valley from the ocean (blue arrows in Figure 1a). Such sea breezes are known to occur in mountainous western Oregon (Banta et al., 2020; Olsson et al., 1973) but may be coupled with other terrain-forced flows in this region of complex mountains and basins. This wind passed through the fire perimeter and smoke-filled valleys to then reach the broad valley containing Merlin and Grants Pass. Thus, the $PM_{2.5}$ late-afternoon spikes could be indicating advection of accumulated low-altitude smoke from the valleys followed by cleaner sea breeze air. Although of interest as a mechanism for part of this analysis, further investigation of the possible sea breeze flow is beyond the scope of this paper and challenging due to the limited observational network in complex terrain.

Solar radiation decreased with greater concentrations of $PM_{2.5}$. Solar noon decreases of 190, 50, and 100 W m^{-2} were observed for the three days shown, respectively, calculated against clear-sky values of 900 W m^{-2} recorded at this site before the Rum Creek fire started. These were cloud-free days. The smoke shading affected the diurnal temperature cycle with maximum temperature at 15:00 local time for the days with greater morning $PM_{2.5}$ concentrations (30 August and 1 September) and earlier, at 14:00, for the clearer morning (31 Aug). There was also a temperature drop each afternoon accompanying the spike in $PM_{2.5}$, decreasing 2.2°C between hourly measurements on both 30 and 31 August and distinct from the sharp diurnal drop at sunset on those days.

Smoke plume properties were retrieved from an overpass of the NASA multi-angle imaging spectrometer (MISR) on 30 August by Noyes and Kahn (2024). They found 558 nm AOD maximum values in excess of 8 within a few tens of km of the fire with values greater than 1 persisting in valleys throughout the region. The MISR overpass occurred at 11:54 local time on 30 August shortly after the PUMAS observations began. Single scattering albedo ranged 0.93–0.99 with the lowest values generally found in the areas of highest AOD. Further details are presented by Noyes and Kahn (2024).

The smoke AOD and other properties undoubtedly underwent substantial variations spatially and throughout the PUMAS observational timespan, but other satellite AOD, for example, from MODIS, is unavailable due to the very high optical depth pixels being filtered out. However, noting the large MISR AOD values and the sharp contrast between opaque smoke and clearer sky (e.g., in Figure 1b) is sufficient for setting up the following discussion, as the optical depth of the smoke in some locations was sufficient to greatly reduce solar insolation at

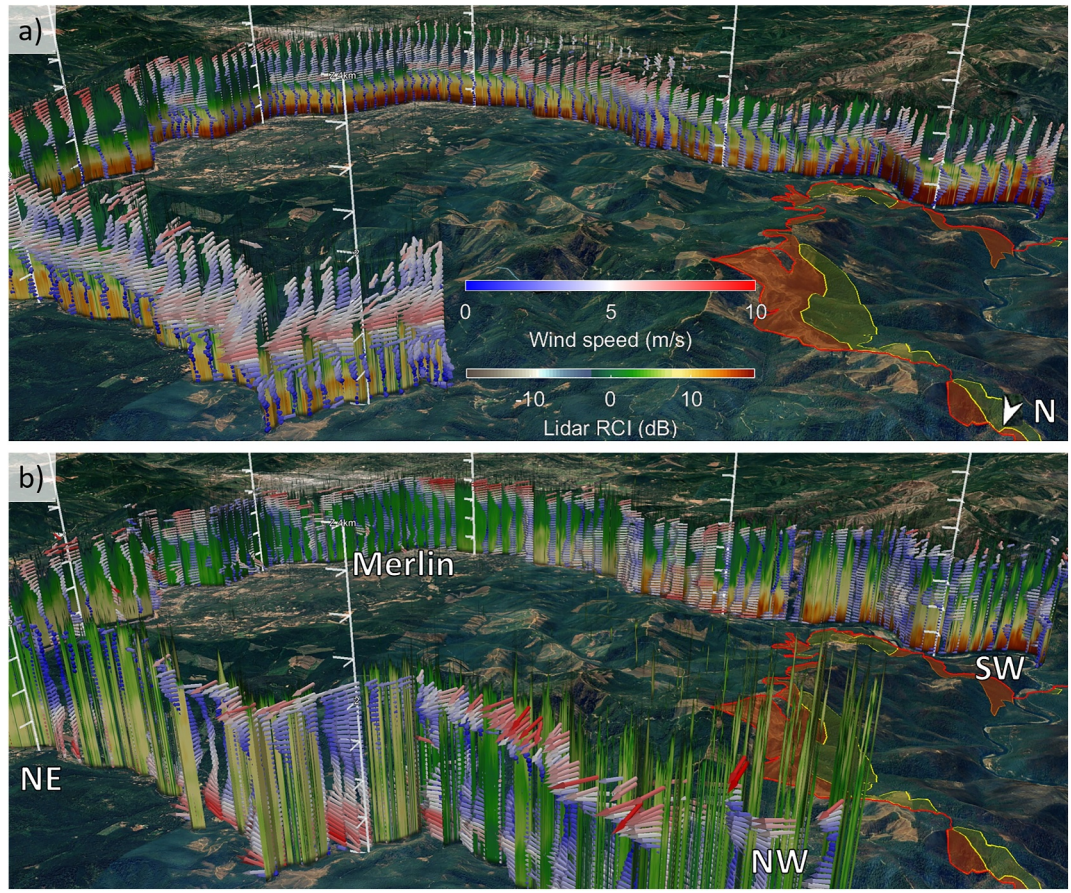

Figure 4. 30 August PUMAS data at Rum Creek along the drive route shown in Figure 1 with key locations noted in panel (b). The fire perimeter is overlaid in the lower right. This tilted viewpoint is from north of the fire. RCI is plotted as a solid curtain and arrows indicate wind speed (with color scale) and direction. White axes are vertical with tick marks every 500 m. (a) 11:10–12:14 local time and (b) 15:27–16:30 local time.

the surface and thus impact dynamics. In the next section, PUMAS RCI will act as a qualitative measure of the smoke columns.

4.2. BL Evolution at the Rum Creek Fire

The PUMAS truck drove the route shown in Figure 1 around the Rum Creek fire on 30 August and 1 September. The fire perimeter occupied a river valley with only one road accessing the north and south ends. These approaches to the fire perimeter were through valleys often with a dense smoke layer confined below the mountaintops (~1 km ASL). The eastern portion of the PUMAS drive route passed through the town of Merlin in much more open and flat terrain where there was often much less smoke due to the distance from the fire and the complex terrain, and dilution in the broader valley. These two areas—valleys near the fire and open terrain farther away—largely corresponded to two distinct regimes in smoke amount and BL dynamics. The PUMAS data for these days are presented in full in Figures 5 and 6. Along with the spatial heterogeneity of smoke amount, large temporal variations were observed. Stagnant conditions around the Rum Creek fire were followed by northwesterly winds on both days though with different timing.

Until midday on 30 August (before 13:00 local time), the whole PUMAS drive route was covered in a thick smoke layer as shown in Figures 4a and 5. As indicated by the PUMAS lidar RCI, the smoke was most dense in the lowest 500 m and in the valleys closest to the fire perimeter accompanied by stagnant winds. This is consistent with past studies of stably stratified smoke-filled valleys that can persist for hours during the day due largely to terrain trapping and the reduced solar insolation that leads to a shallower BL (Garratt et al., 1990; Kochanski et al., 2019; Robock, 1991). Above 1 km there was very little aerosol (low RCI). Four hours later, in Figure 4b, the

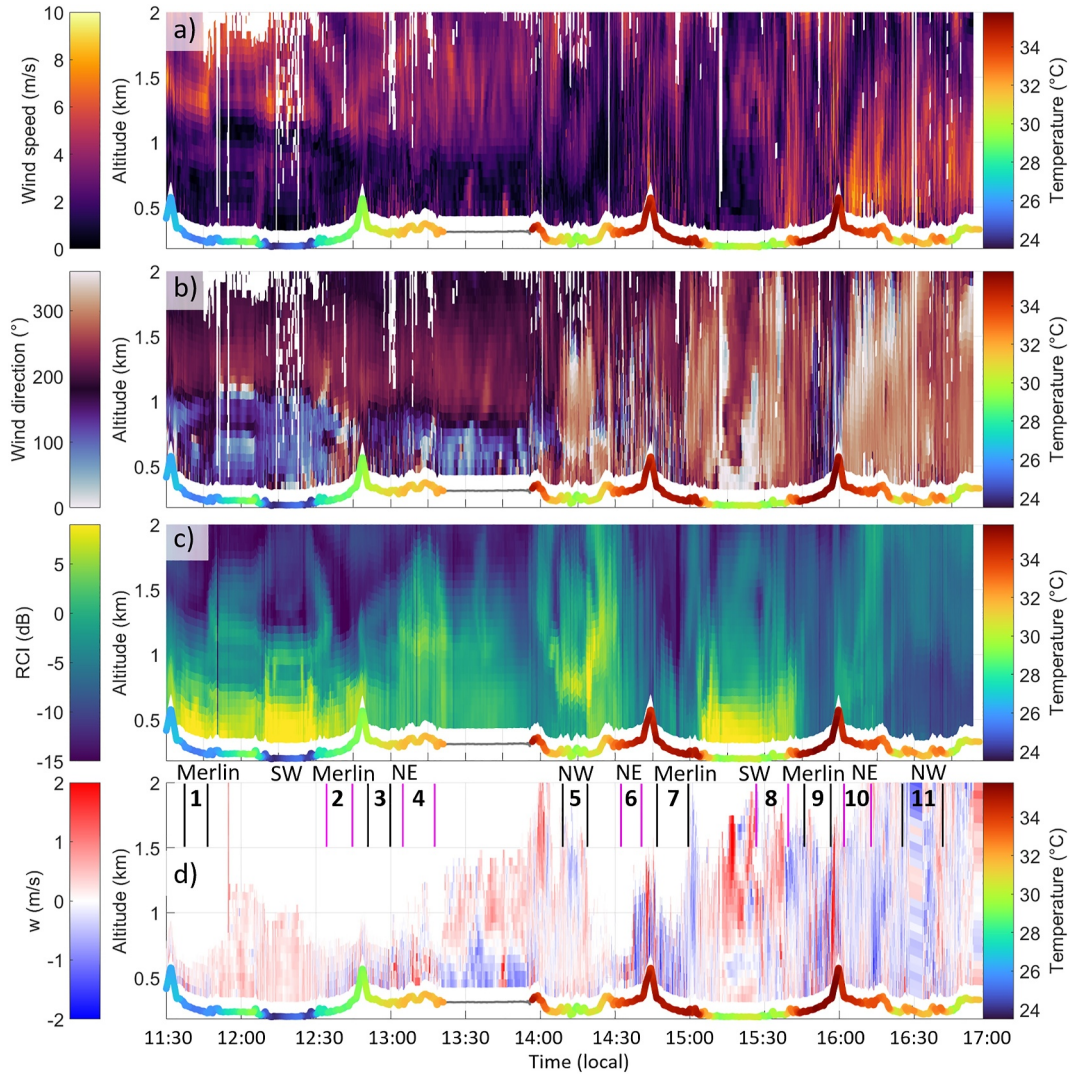

Figure 5. PUMAS lidar (a) wind speed, (b) wind direction, (c) RCI, and (d) vertical velocity at the Rum Creek fire on 30 August. The PUMAS in situ air temperature data (T_{3m}) is plotted at the terrain height. Key locations on the repeated transect, as indicated in Figure 1, are noted above (d). Numbered segments used for analysis are delineated in (d) with alternating black and pink for visual clarity.

shallow smoke layer was not present over the Merlin and NW areas, though SW still had a thick smoke layer. Two main factors likely contributed to this reduction in smoke concentrations. One, the transition to northwesterly flow likely pushed out much of the stagnant accumulated smoke. Under this regime, the SW area was directly downwind of the fire perimeter and was still inundated with smoke. Two, the relatively constant RCI versus height over Merlin, NE, and NW at this time indicates that the smoke was well-mixed over a deeper layer likely due to solar insolation and deepening of BL convective turbulence. This is consistent with Figure 5, which shows warmer temperatures and less smoke initially in the open terrain than the valleys closest to the fire, favoring greater surface heating and convective BL development.

The winds contrasted sharply between these two times. Winds in the smoke layer in the morning and midday were very weak (generally <2 m/s) and southeasterly, while above 1 km (above the mountaintops), there were southwesterly speeds >5 m/s. In the afternoon, the low-altitude wind in the valleys shifted to northwesterly and strengthened to 5–8 m/s. This is the possible sea breeze mentioned in Section 4.1. The afternoon persistence of enhanced RCI at SW is consistent with the northwesterly winds pushing high concentrations of smoke from

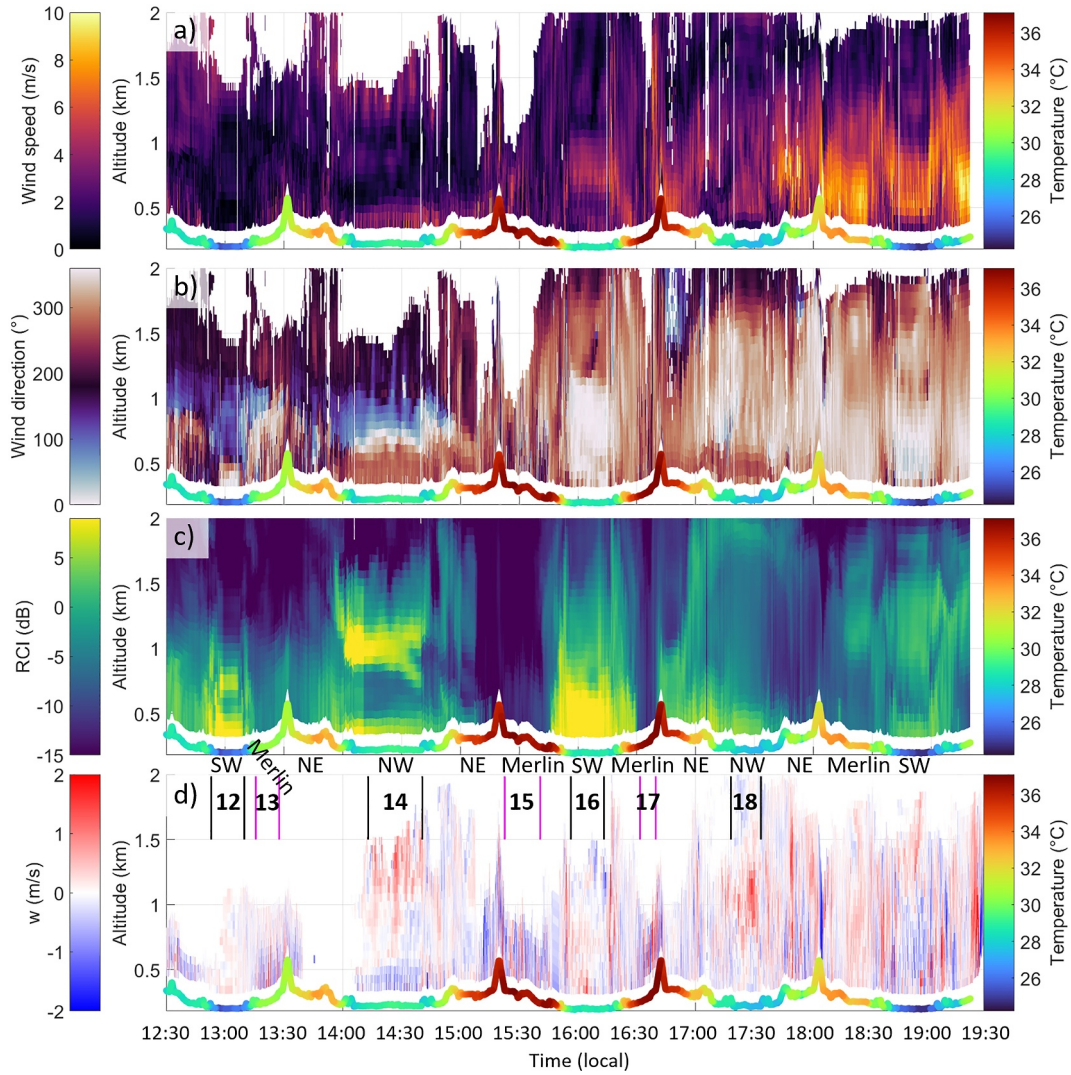

Figure 6. As in Figure 5, but for 1 September.

within the fire perimeter through the narrow valley before reaching the relatively open terrain around Merlin where it could dilute.

On 1 September, similar afternoon northwesterly wind was observed though the morning had less smoke built up in the valleys. The wind shift occurred around 14:00 local time on both observation days, and this is further emphasized in Figures S2 and S3 in Supporting Information S1. A preliminary discussion of this 1 September case and a plot of the PUMAS and airborne lidar data were presented by Carroll et al. (2024, their Figure 4). Strobach et al. (2024) focused on buoyant updraft plume dynamics from 16:30–17:00 local time that day. They included plots of the airborne lidar data and discussion of the plume dynamics within and west of the fire perimeter as well as additional discussion of the larger-scale meteorological conditions. Airborne lidar data are not shown in this study as it had much less coverage than PUMAS in the relevant valleys.

On both days, the mountain pass between NW and SW on the drive route had very little smoke and greater temperatures, as the smoke concentrated in the lower valley floors. This pass is noticeable as the peak above 500 m in Figures 5 and 6 and heading north from Merlin in Figure 1.

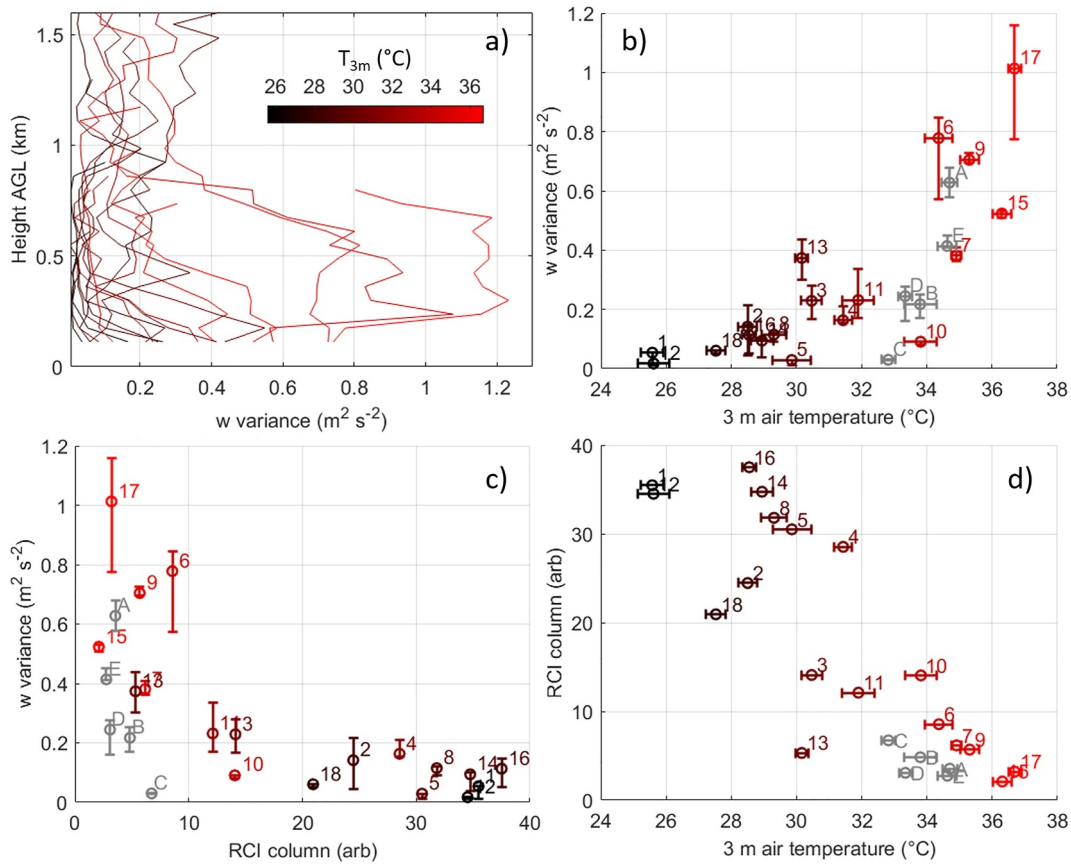

Figure 7. Subsets of PUMAS data from 30 August and 1 September (Rum Creek) colored by the average T_{3m} from that timespan and from 5 September (Mountain) in gray. (a) Vertical velocity variance profiles (excluding 5 September—see Figure 11). (b, c) Each profile $\overline{w'^2}$ averaged over 0.1–0.4 km AGL and plotted as a function of (b) T_{3m} and (c) range-corrected intensity (RCI) summed over 0–3 km. Bars on the averaged $\overline{w'^2}$ represent the range after removing the single greatest and least values (as a means of outlier removal). T_{3m} bars are standard deviation within the timespan that $\overline{w'^2}$ was calculated. (d) Average T_{3m} versus column RCI.

4.3. Smoke Shading Impacts on Temperature and BL Mixing

We now turn our attention to the PUMAS lidar profiles of $\overline{w'^2}$ as a measure of turbulent mixing in the BL and the T_{3m} and RCI as they correlate with smoke shading.

Among the selected data, the temperature range observed by PUMAS on each day was 25.1–35.8°C and 24.7–37.0°C, respectively, on 30 August and 1 September. Although this range is partly from the diurnal temperature cycle, the changes of several °C over very short drive times (distances often <5 km as will be shown later) exemplify the sharp thermal gradients that can develop from smoke shading. Figures 5 and 6 show that these changes in T_{3m} correlate with the strength of vertical motions in the BL and with RCI. Figure 7 explores these relationships qualitatively, since there is no theoretical functional expression to apply for these variables. It should also be noted that some fraction of this temperature difference could be due to changes in elevation, surface type, and river proximity though the exact potential contribution of such effects is undetermined.

The PUMAS drives at the Rum Creek Fire were subdivided by manual inspection into segments with temporally constant RCI profiles as seen in Figures 5 and 6 (exact times are listed in Table S1 in Supporting Information S1). The median RCI profile for each timespan was column-integrated from 0 to 3 km AGL to provide a single proxy value for column smoke amount (most smoke was below 3 km), since more direct measurements of smoke shading such as downwelling solar radiation or AOD were not available. For the same time segments, the average and standard deviation of T_{3m} and a profile of $\overline{w'^2}$ from the vertically staring lidar beam were calculated.

The $\overline{w'^2}$ profiles are plotted in Figure 7a colored by the average T_{3m} for that $\overline{w'^2}$ calculation timespan. The $\overline{w'^2}$ profiles spanned two orders of magnitude ranging from almost no turbulent mixing for lower T_{3m} to values typical of a clear-sky convective BL with the greatest T_{3m}. Interestingly, the depth of the BL (indicated by a sharp decrease in the $\overline{w'^2}$ profile) remained fairly shallow never exceeding 900 m on these days. This is possibly due to the reduced solar insolation from smoke shading, but more observations of the BL depth in this area would be needed to confirm. Complex terrain could also be playing a role in BL structure, for example, the greater temperatures observed at the high mountain pass could generate upslope flows.

Figures 7b and 7c show the $\overline{w'^2}$ profiles for the selected data segments averaged from 0.1 to 0.4 km AGL and plotted against T_{3m} and column RCI. 0.1–0.4 km was chosen for the $\overline{w'^2}$ average because in some cases, there was little data or a sharp change above 0.4 km, thus this layer best shows the trends for this data set. The average $\overline{w'^2}$ increased with T_{3m}, and decreased with column RCI. These relationships are quite consistent despite the spatiotemporal changes in smoke throughout the region and the limitations of using column RCI instead of a more direct quantitative measure of smoke shading. The relationship between column RCI and T_{3m} was not as strong as shown in Figures 7c and 7d.

The diurnal temperature cycle is apparent in these data, but the sharp spatial gradients caused by smoke shading dominated the effects highlighted here. In clear contrast to the diurnal cycle, segment 16 was at the peak in the diurnal temperature cycle yet it had greatly subdued temperature and mixing due to smoke shading contrasting the adjacent clearer-sky segments 15 and 17. Also, the first measurements each day (segments 1, 12) were the coldest but were also the most heavily smoke shaded due to stagnant accumulation of smoke overnight and the next legs with less smoke were consistent with the observed relationships having greater $\overline{w'^2}$ and 2–5°C warmer (e.g., segments 2, 3, 13).

5. Smoke-Induced Density Currents

This section examines dynamic outcomes of the differential shading and induced temperature gradients. Two cases are presented that both feature a cold smoky air mass and a sharp leading frontal edge: one at the Mountain fire that follows standard density current theory and one at the Rum Creek fire that does not.

5.1. Smoke-Induced Density Current Opposing the Ambient Flow at Mountain Fire

On 5 September at the Mountain fire, PUMAS took the drive route shown in Figure 2 along the western edge of the basin downslope from the fire. This drive track of interest consisted of two temporally separated legs: one from 15:15–15:36 local time and the other from 17:11–17:37. The break between these legs is noted in Figure 2 and indicated with a vertical green line in Figure 8. During the time gap, PUMAS was scouting potential locations for the next day's measurements in the complex terrain to the west. The data from that time were deemed irrelevant for this study as it was off-track and substantially influenced by the complex terrain.

Figure 8 shows the PUMAS lidar winds and RCI for the drive route passing from mostly clear sky (segment A, 0–12 km) into a smoke-shaded region (B, C, D; 12–56 km) and then into clear sky again (E, 56–64 km). Southwesterly winds aloft advected the main smoke plume over segment B. The southern half of the track crossed the valley mouth where smoky outflow would be expected, as smoke shading prompted a temperature gradient strong enough to initiate downslope drainage (valley indicated in Figure 2). Smoke layers at varying altitudes are evident in the RCI. The smoke-shaded region is also apparent in the T_{3m} data.

The southern half of the route (segments C, D, E) captures what appears to be a cold smoke density current likely originating from the main drainage valley previously indicated. Smoky northwesterly flow with 3.5 m/s wind speed undercut an air mass moving in from the southeast with 6 m/s wind speed. T_{3m} within the smoky air mass was substantially colder than the ambient temperature of segment E with a range of 3.0°C that was undoubtedly caused by smoke shading. At the leading edge of the density current (between segments D–E), an updraft was observed with the PUMAS vertical channel reaching a max of 2.7 m/s and spanning 1.0 km along-track. Updraft depth was at least 950 m but cannot be precisely reported due to loss of the lidar signal at higher altitudes.

Both the RCI and the T_{3m} indicate two distinct fronts and feature a sharp gradient in RCI and T_{3m} despite having similar winds. We will call the farthest front (at 56 km in Figure 8) the "first front" and the other (at 45 km) the "second front." The similar wind profiles behind both fronts suggest that there is no clearly propagating density

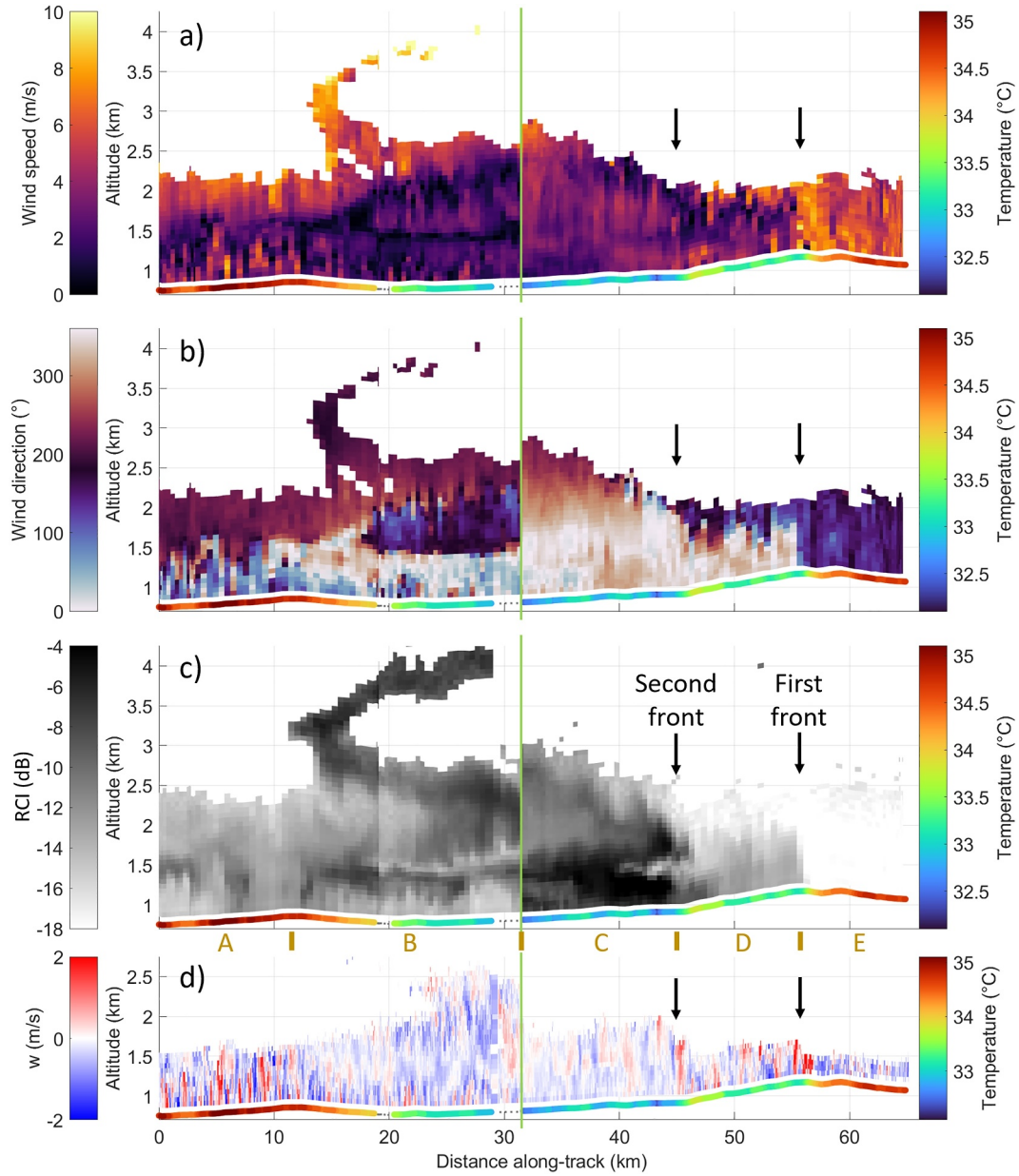

Figure 8. PUMAS lidar (a) wind speed, (b) wind direction, (c) range-corrected intensity (RCI), and (d) vertical velocity for the Mountain fire plume transect on 5 September, shown in Figure 2. T_{3m} is plotted at the terrain height. The horizontal axis starts at the north end of the route, and the green line at 32 km denotes the 95-min temporal break. Yellow letters and bars above (d) indicate segments as noted in Figure 2. There is a change in RCI around 19 km due to a reduction in output power.

current associated with the second front overtaking the first though information is limited with just this one transect. The sharp RCI gradient of the second front may be due to heterogeneous smoke distribution and buildup before flowing into the observation area; such heterogeneity could also explain the slight difference in temperature (0.4°C) between the two fronts. The directional wind shear and density differences at the edges of the density current likely contributed to the wave-like structure in RCI at 40–45 km in Figure 8. The terrain may also have played a lesser role in the observed features, as there were low hills along the drive route south of the second front. It is also possible that the weak stationary front in the area contributed to the opposing flows and warm southerly winds, but Figure 8 does provide clear evidence of localized smoke shading cooling and not a uniformly cool frontal air mass.

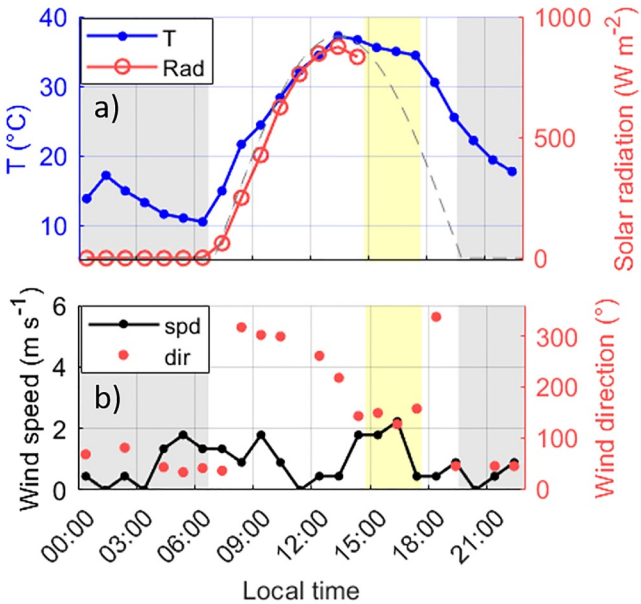

Figure 9. MSAC1 Remote Automatic Weather Stations site data on 5 September, (a) 2 m air temperature and solar radiation and (b) 6 m wind speed and direction. Gray dashed line is a cloud-free solar radiation reference line. Gray shading is nighttime and yellow shading is the PUMAS observation period.

Figure 9 shows data from the Mt. Shasta RAWS site MSAC1, which was located at the southern end of the PUMAS route (Figure 2 map). From 08:00–12:00 local time, the wind was weak and northwesterly before shifting to southeasterly at 14:00, which persisted throughout the PUMAS observation timespan. This southeasterly wind was the clean air mass encountered at the end of the PUMAS route, and it is possible that this air mass advanced farther north during the 4 hr it persisted before receding against the smoky air mass. The shift to very weak northeasterly wind at sunset was likely a diurnal terrain-influenced flow pattern as evidenced by the sharply dropping temperature and appearance of this flow on other nights. It is possible that the smoke front reached MSAC1 with the northwesterly wind just after 18:00, but there is no data available that can confirm this.

The MSAC1 temperature changed by less than 0.4°C over the timespan of PUMAS legs C, D, and E, indicating a decent steady-state approximation for the transect. The MSAC1 temperature at 18:00 was 34.4°C, only a 0.2°C difference from the nearest PUMAS measurement. The solar radiation measurement at this site was blocked in the afternoon, so no insight into smoke shading magnitude can be given.

5.1.1. Mountain Fire Density Current Analysis

A common method to confirm the existence of a density current flow is to use the density current propagation speed equation

$$V_{DC} \cong k\sqrt{\left(\frac{T_a - T_{DC}}{T_a}\right) gh} - bV_a \quad (1)$$

where V_{DC} is the density current propagation speed, k is the Froude number, T_a is the ambient temperature, T_{DC} is the cold-side temperature, g is the gravitational acceleration constant, h is the depth of the density current, b is an empirical constant, and V_a is the ambient wind speed directed opposite to the density current propagation (Simpson & Britter, 1980). Density currents in the atmosphere can be identified by solving for k and getting a result of ~0.7–1.2 (Kingsmill & Crook, 2003; Wakimoto, 1982). Because there was only one PUMAS transect of the front, we are unable to directly estimate V_{DC} via propagation over time to then solve for k. Instead, we can confirm that the observed flow is consistent with a density current by solving for V_{DC}, assuming typical parameters for a density current and checking that the measured wind speed behind the front is equal to or greater than the calculated V_{DC}. If so, then smoky air is being transported toward the front, which is a fundamental property of density currents.

Equation 1 values for the first front are given in Table 1 (T_a and T_{DC} are averages from 59 to 64 km and 48–54 km in Figure 8, respectively). A range of values for k and b are found in the literature for both laboratory and atmospheric studies of density currents (Kingsmill & Crook, 2003; Lareau & Clements, 2015; Simpson & Britter, 1980; Wakimoto, 1982). Calculating a low and a high estimate for V_{DC} based on this range of values in Equation 1 yields $V_{DC} = -1.9$ m/s to 2.2 m/s. This range of V_{DC} indicates that the smoke-filled front may have stalled or begun retreating by the time of the observations. The fairly strong ambient winds directly opposing the smoky

Table 1
Input and Output Parameters for the Density Current Equation 1 Across the Smoke Front Transect at the Mountain Fire (5 September) and Two at the Rum Creek Fire (1 September)

	T_{DC} (°C)	T_a (°C)	h (m)	V_a (m/s)	k low, high	b low, high	V_{DC} calc low (m/s)	V_{DC} calc high (m/s)
5 September	33.1	34.6	630	6.0	0.77, 1.1	1, 0.62	−1.9	2.2
1 September first	28.9	36.2	360	0			7.1	10.1
1 September second	27.9	35.8	420	−1.9			9.8	12.5

Note. Low and high estimates of calculated V_{DC} (V_{DC} calc low, high) use the corresponding k and b values.

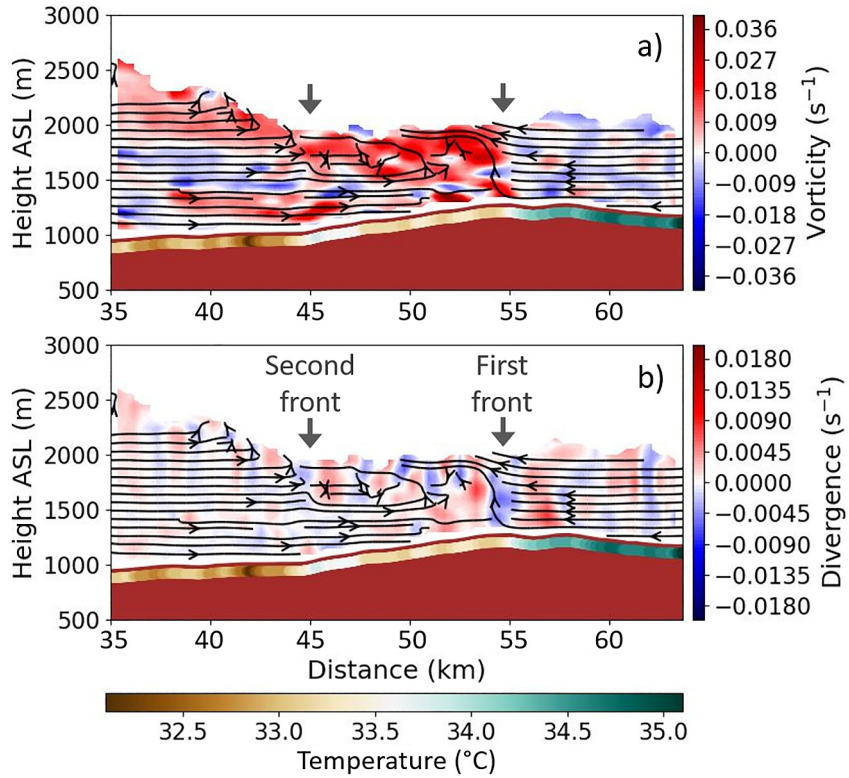

Figure 10. PUMAS data at the density current on 5 September (35–64 km in Figure 8). Black arrows are streamlines of the in-plane winds along the drive route. Color is (a) vorticity and (b) divergence. T_{3m} is plotted at the surface.

flow play a major role in this. In the absence of ambient winds, the V_{DC} range would be 4.1–5.9 m/s. The only other PUMAS data here on this day, 4 hr prior (13:10–13:20 local time), had light and variable winds (<2 m/s with inconsistent direction), which agrees with the MSAC1 data. This indicates that the smoky air mass could have spread more quickly as a density current before being retarded by strong ambient winds by the time of observation. It is also possible that the density current traveled more quickly in the confined valley before reaching the open terrain where the observations were made following mass continuity with velocity over a given cross-sectional area (Bernoulli's Principle).

5.1.2. Vorticity, Divergence, and $\overline{w'^2}$ Across the Mountain Fire Density Current

Figure 10 shows streamlines of the along-track wind across the smoke fronts (35–64 km in Figure 8) overlaid on plots of vorticity and divergence. The vorticity and divergence were calculated along the plane of lidar observations. Analyzing the along-track winds in this way is appropriate in this case, as PUMAS was driving approximately with the wind in the smoke front and against the wind in the ambient air mass, that is, the winds were all in-plane with the drive track.

The streamlines show the opposing flows and the lifting of the ambient air mass at the first front. As the warmer air mass rode atop the density current head structure, directional shear generated vortices along a rising trajectory between 1,500 and 2,000 m ASL. Greater values of positive vorticity were found at the shear interface consistent with the streamlines. Several distinct vortices were present, though their extent was not fully captured as the lidar signal was lost outside of the smoky entrainment zone. These vortices coincided with minima in horizontal wind speed (Figure 8a). Relatively low and disorganized values of vorticity were present elsewhere.

Negative divergence at the first front indicates convergent lifting, and the divergence just upwind on the ambient side indicates an accelerating flow into the updraft region. There was a smaller divergence enhancement on the smoky side of the first front as well. There was no clear evidence of the second smoke front in these dynamics plots, aside from the minor updraft kink in the streamlines at 45 km.

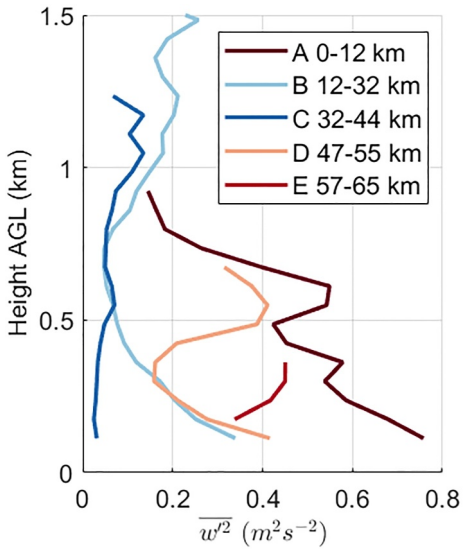

Figure 11. Vertical velocity variance ($\overline{w'^2}$) profiles calculated from the PUMAS lidar data at the Mountain fire. Each $\overline{w'^2}$ profile was calculated using the data span defined in the legend corresponding to the segments in Figures 2 and 8d.

Figure 11 presents the $\overline{w'^2}$ profiles from the five distinct segments of the drive transect. The results agree with the findings for Rum Creek from Section 4.3. The most heavily smoke-shaded and cold segment (C, behind the second front) had very low $\overline{w'^2}$ throughout the profile, and the greatest $\overline{w'^2}$ occurred in A, the hot unshaded first segment of the transect. A lack of aerosol outside the smoke layer stunted the vertical extent of the profiles for D and E, though an aloft peak was seen in D behind the first front ~500–600 m AGL. This was caused by strong wind shear generating turbulence at the interface of the density current and opposing ambient flow. The B profile is also interesting as it indicates a shallow weakly turbulent BL also evident in Figure 8. This is likely a diminished convective BL due to the recent introduction of smoke shading from the aloft plume, which was not present in the late morning (e.g., Figure 2b). The shading in B was either recent enough or weak enough that there was some continued convective turbulence.

Figure 7 includes the scatterplots for these Mountain fire segments. The same trends were present as for the Rum Creek data, though the Mountain fire data spans a much smaller range of temperature and RCI. This is for two main reasons. One, the Mountain fire observations were taken over a shorter time span, and thus there was less time for changing background conditions. Two, Mountain fire smoke only moved east of the fire in the afternoon, and thus the smoke generated a perturbation on hot clear-sky afternoon conditions. This is a stark contrast to Rum Creek, which had several days of smoke production and overnight stagnant buildup. It is important to note again that RCI is not an absolute measurement but is dependent on the lidar output power. Thus, the relatively low RCI column values for the Mountain fire in Figure 7 may be a combination of less smoke than Rum Creek (no stagnant buildup) and the lidar power drift between observing the Rum Creek and Mountain fires.

5.2. Smoke Front Aligned With Ambient Flow at Rum Creek Fire

PUMAS drove in and out of smoky regions several times on both days of sampling at the Rum Creek fire though only one clear instance of a propagating smoke front was found in the data. Figure 12 shows data from a drive into and then immediately out of the smoky southern valley (between SW and Merlin in Figure 1) on 1 September spanning 15:39–16:31 local time. Although persistent northwesterly winds were observed in this valley on both days, this case occurred before that time.

The RCI in Figure 12 shows a smoky air mass initially confined below 1 km that extended and flattened by the second transect. Both transects captured a sharp RCI gradient at the leading edge of the smoky air mass. The first transect shows some convergence at the smoke front and movement of the smoky air mass (consistent weak westerlies pushing into the light and variable ambient winds). This was enhanced during the second transect including stronger wind speeds within the smoky layer more clearly suggestive of a density current. A difference in T_{3m} of 8°C was observed during both transects with 5.8°C of that change occurring over just 5 km on the first transect though the temperature gradient was several kilometers behind the smoke front. An updraft at the leading edge was present though weaker than the Mountain fire case due to the opposed versus same directions of ambient flow. The updraft in the first transect was fragmented into two closely clustered updrafts with a maximum w of 2.0 m/s, a width of 500 m, and a depth of 300 m (though weaker updraft <0.8 m/s persisted to 750 m). The fragmenting may have been caused by turbulent overturning or terrain features in the narrow valley. On the second transect, there was one contiguous updraft at the smoke front with a max of 1.1 m/s, 300 m width, and 500 m depth.

Greater values of w were present in the smoky air mass from ~2 to 4 km on both transects because PUMAS passed within 200 m of an isolated small area of flames. This also caused variable wind speed and direction around the same time. The vicinity of the rest of the drive route was not yet burned, so it is unlikely that active flames played a direct role in the other dynamics discussed here. This was the closest the PUMAS truck came to active flames during CalFiDE and the only such instance of obvious turbulence enhancement due to flame proximity.

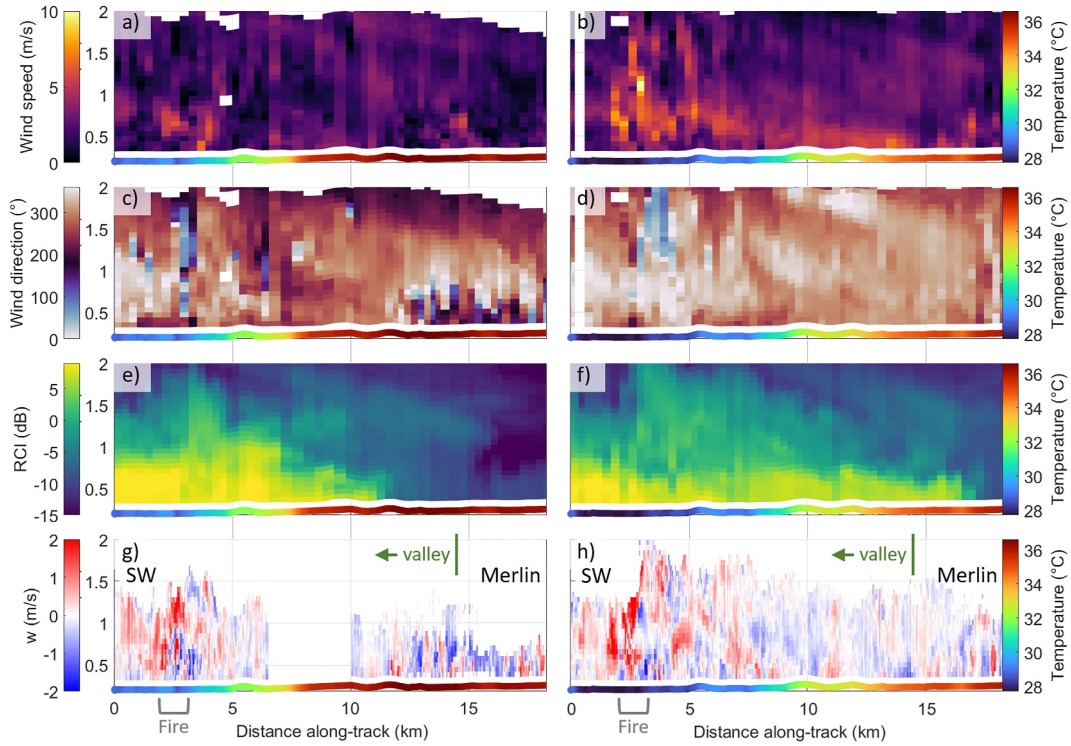

Figure 12. PUMAS data on 1 September at Rum Creek (a, c, e, g) driving into the smoky valley from 15:39–16:05 local time and (b, d, f, h) driving out of the valley from 16:05–16:31. Rows from top to bottom are (a, b) wind speed, (c, d) wind direction, (e, f) RCI, and (g, h) w. T_{3m} is plotted at the terrain height. Closest proximity to the fire is indicated at the bottom.

5.2.1. Rum Creek Smoke Flow Not Consistent With Density Current Theory

The smoke front intercepts occurred 5.6 km and 44 min apart with acceleration of the smoky air mass wind speed during that time. Because of this substantial acceleration, we do not have sufficient information to calculate a representative V_{DC} directly from the smoke front propagation.

Using typical density current values of k to calculate V_{DC} as was done for the Mountain fire case indicates that this smoke front did not follow a standard density current evolution. For both transects, the observed wind speed within the smoky air mass (maximum 6.0 m/s, on the second transect) was much less than the theoretically calculated V_{DC}, which ranged from 7.1 to 12.5 m/s. Table 1 cases "first" and "second" correspond to the left and right columns of Figure 12, respectively.

The complex terrain likely played a major role in impeding the formation of a standard density current which would have propagated much more quickly. This transect along the river valley floor had multiple turns that obscured line of sight; a straight clear line of sight is only possible above ∼150 m, which is coincidentally similar to the PUMAS lidar lowest observed altitude (120 m). The protruding mountain slopes would act to impede any flow acceleration, and the blockage and subsequent turbulent or varying flow could also be a major factor in the ∼5 km breadth of the temperature gradient. It is also reasonable that under these constraints, the near-surface temperature gradient would lag behind the smoke at the PUMAS lidar observation altitudes, and this is seen in Figure 12. The temperature gradient only moved 3.7 km between transects using the change in the 32°C location, as it was roughly the midpoint temperature. This is 66% of the smoke front propagation distance. Unfortunately, we are unable to further characterize impedance of the low-level flow with the available data. This contrasts the Mountain Fire case where the density current was observed in relatively flat open terrain.

The open valley to the north of the fire perimeter may also have played a role in the observed dynamics. Unlike the Mountain Fire case, which had one clear drainage valley from the ridgeline burn area, the Rum Creek fire took place in a valley with open ends to the north and south. This could have added additional forcing mechanisms

(e.g., additional thermal gradients to the north) to the low-level winds in the area that we are unable to quantify, since the PUMAS route did not reach the northern valley entrance.

6. Conclusions

These observations exhibit the localized cooling effects of smoke shading and the subsequent impacts on local BL dynamics adding to the sparse record of observations in the literature. Near-surface air temperature exhibited sharp gradients between smoky and clear-sky air masses up to 1.0°C over 2 km in relatively open terrain (Mountain fire) and 3.3°C over 2 km in complex terrain (Rum Creek fire).

A case study at the Rum Creek fire featured smoke-filled valleys with stagnant winds and thick smoke confined below 500 m that persisted through early afternoon. The smoke eventually cleared with winds possibly indicative of a sea breeze coming up the river valley, and the remaining lower concentrations of smoke were mixed over a deeper layer. Nearby $PM_{2.5}$ observations indicate that this diurnal wind pattern may have caused significant smoke advection on many days.

Examining profiles of vertical mixing ($\overline{w'^2}$) showed correlation between the smoke-shaded cooler surface temperatures and inhibition of daytime convective turbulence. Turbulent BLs were only observed in the warmest areas with relatively little smoke and even then the BLs remained shallow throughout the day (<1 km AGL). Some shallow BL convective turbulence was present over newly or weakly shaded areas.

The temperature gradients also resulted in thermally driven flows, including one case that fell within standard density current theory at the Mountain fire. The unique PUMAS lidar data set provided horizontal and vertical wind measurements while underway enabling calculation of streamlines, vorticity, and divergence to show the shear vortices atop the density current and convergent lifting at the leading edge. At the Rum Creek fire, a strong thermal gradient did aid in acceleration and propagation of a smoke front but it was slower than predicted by density current theory. This was likely due to inhibition by complex terrain in the meandering river valley, which could have also contributed the near-surface temperature gradient lagging behind the smoke front where it was observed >120 m above the surface.

The two fires also exhibited vastly different conditions in which smoke shading can occur; the Rum Creek observations had preceding days of smoke emissions and stagnant accumulation overnight, whereas the Mountain fire transect smoke shading was a perturbation introduced in the afternoon of a warm clear-sky day resulting in different meteorological impacts and temperature anomalies. On other occasions not detailed here, flows opposing thermal gradients were observed indicating the importance of understanding the superposition of larger-scale forcing mechanisms or diurnal flow patterns in the complex terrain. Predicting such smoky air mass flows is important for air quality and fire management, though we still need to improve our understanding of such events with observations and improve modeling capabilities regarding fire-atmosphere couplings and smoke radiative properties.

Although this study did provide new observations of smoke shading and BL dynamics around fires, it was an opportunistic analysis from a campaign that was not designed primarily for this purpose. The study would have benefited from additional measurements. For example, temperature is not an ideal surface measurement for assessing smoke shading. Downwelling radiative flux relates more directly to both the smoke shading and the BL convective turbulence and is a key variable in models unlike RCI. Temperature profiling would also be informative to better describe the inversions created or strengthened by smoke shading and the eventual breakup of that inversion. A denser observational network would have also been informative to provide measurements when and where PUMAS was not operating, including radiative flux, $PM_{2.5}$, ozone or other species relevant for air quality, and winds. This is a common limitation in remote areas where wildfires often occur. However, in the absence of a dense network, mobile platforms have great advantages emphasized in this study for capturing variability and horizontal gradients with just one instrument package.

Modeling studies can also provide insights into smoke shading especially with the ability to isolate key variables. For example, the temperature variations at Rum Creek were heavily affected by smoke shading but were also undoubtedly modified to some degree by the diurnal cycle and topographic and hydrologic factors. A modeling study could better inform the independent mechanisms of smoke shading and the coupled impacts with time of day and local features both for the formation of gradients and resulting dynamics.

Data Availability Statement

Data from CalFiDE, including the PUMAS lidar data used here, are archived on the NOAA Chemical Sciences Laboratory web page: NOAA Chemical Sciences Laboratory (2022, https://csl.noaa.gov/groups/csl7/measurements/2022calfide/). The $PM_{2.5}$ from the Oregon Dept. of Environmental Quality site in Grants Pass was downloaded via the EPA Air Quality System (US EPA, 2024), and the RAWS and NWS station data were accessed via the University of Utah MesoWest (https://mesowest.utah.edu/) though other archives of these data are available online as well.

Acknowledgments
CalFiDE measurements and analysis were supported in part by NOAA Cooperative Agreements NA17OAR4320101 and NA22OAR4320151 as well as Public Law 117-43 Disaster Relief Supplemental Appropriations Act signed 30 September 2021 including $55M (ORF) related to the consequences of hurricanes and wildfires. The statements, findings, conclusions, and recommendations are those of the authors and do not necessarily reflect the views of NOAA or the US Department of Commerce.

References

Banta, R. M., Pichugina, Y. L., Brewer, W. A., Choukulkar, A., Lantz, K. O., Olson, J. B., et al. (2020). Characterizing NWP model errors using Doppler-lidar measurements of recurrent regional diurnal flows: Marine-air intrusions into the Columbia River Basin. *Monthly Weather Review*, *148*(3), 929–953. https://doi.org/10.1175/mwr-d-19-0188.1

Bernstein, D. N., Hamilton, D. S., Krasnoff, R., Mahowald, N. M., Connelly, D. S., Tilmes, S., & Hess, P. G. (2021). Short-term impacts of 2017 western North American wildfires on meteorology, the atmosphere's energy budget, and premature mortality. *Environmental Research Letters*, *16*(6), 064065. https://doi.org/10.1088/1748-9326/ac02ee

Bian, Q., Ford, B., Pierce, J. R., & Kreidenweis, S. M. (2020). A decadal climatology of chemical, physical, and optical properties of ambient smoke in the western and southeastern United States. *Journal of Geophysical Research: Atmospheres*, *125*(1), e2019JD031372. https://doi.org/10.1029/2019jd031372

Bonin, T. A., & Brewer, W. A. (2017). Detection of range-folded returns in Doppler lidar observations. *IEEE Geoscience and Remote Sensing Letters*, *14*(4), 514–518. https://doi.org/10.1109/lgrs.2017.2652360

Bonin, T. A., Carroll, B. J., Hardesty, R. M., Brewer, W. A., Hajny, K., Salmon, O. E., & Shepson, P. B. (2018). Doppler lidar observations of the mixing height in Indianapolis using an automated composite fuzzy logic approach. *Journal of Atmospheric and Oceanic Technology*, *35*(3), 473–490. https://doi.org/10.1175/jtech-d-17-0159.1

Bonin, T. A., Choukulkar, A., Brewer, W. A., Sandberg, S. P., Weickmann, A. M., Pichugina, Y. L., et al. (2017). Evaluation of turbulence measurement techniques from a single Doppler lidar. *Atmospheric Measurement Techniques*, *10*(8), 3021–3039. https://doi.org/10.5194/amt-10-3021-2017

Bowman, D. M., Balch, J. K., Artaxo, P., Bond, W. J., Carlson, J. M., Cochrane, M. A., et al. (2009). Fire in the Earth system. *Science*, *324*(5926), 481–484. https://doi.org/10.1126/science.1163886

Carroll, B. J., Brewer, W. A., Strobach, E., Lareau, N., Brown, S. S., Valero, M. M., et al. (2024). Measuring Coupled Fire–Atmosphere Dynamics: The California Fire Dynamics Experiment (CalFiDE). *Bulletin of the American Meteorological Society*, *105*(3), E690–E708. https://doi.org/10.1175/bams-d-23-0012.1

Clements, C. B., Lareau, N. P., Kingsmill, D. E., Bowers, C. L., Camacho, C. P., Bagley, R., & Davis, B. (2018). The rapid deployments to wildfires experiment (RaDFIRE): Observations from the fire zone. *Bulletin of the American Meteorological Society*, *99*(12), 2539–2559. https://doi.org/10.1175/bams-d-17-0230.1

Colbeck, I., Atkinson, B., & Johar, Y. (1997). The morphology and optical properties of soot produced by different fuels. *Journal of Aerosol Science*, *28*(5), 715–723. https://doi.org/10.1016/s0021-8502(96)00466-1

Garratt, J. R., Pittock, A. B., & Walsh, K. (1990). Response of the atmospheric boundary layer and soil layer to a high altitude, dense aerosol cover. *Journal of Applied Meteorology*, *29*(1), 35–52. https://doi.org/10.1175/1520-0450(1990)029<0035:rotabl>2.0.co;2

Goodrick, S. L., Achtemeier, G. L., Larkin, N. K., Liu, Y., & Strand, T. M. (2012). Modelling smoke transport from wildland fires: A review. *International Journal of Wildland Fire*, *22*(1), 83–94. https://doi.org/10.1071/wf11116

Hobbs, P. V., Reid, J. S., Kotchenruther, R. A., Ferek, R. J., & Weiss, R. (1997). Direct radiative forcing by smoke from biomass burning. *Science*, *275*(5307), 1777–1778. https://doi.org/10.1126/science.275.5307.1777

Jaffe, D. A., & Wigder, N. L. (2012). Ozone production from wildfires: A critical review. *Atmospheric Environment*, *51*, 1–10. https://doi.org/10.1016/j.atmosenv.2011.11.063

Kingsmill, D. E., & Crook, N. A. (2003). An observational study of atmospheric bore formation from colliding density currents. *Monthly Weather Review*, *131*(12), 2985–3002. https://doi.org/10.1175/1520-0493(2003)131<2985:aosoab>2.0.co;2

Kochanski, A. K., Mallia, D. V., Fearon, M. G., Mandel, J., Souri, A. H., & Brown, T. (2019). Modeling wildfire smoke feedback mechanisms using a coupled fire-atmosphere model with a radiatively active aerosol scheme. *Journal of Geophysical Research: Atmospheres*, *124*(16), 9099–9116. https://doi.org/10.1029/2019jd030558

Langford, A. O., Senff, C. J., Alvarez, R. J., Aikin, K. C., Ahmadov, R., Angevine, W. M., et al. (2023). Were wildfires responsible for the unusually high surface ozone in Colorado during 2021? *Journal of Geophysical Research: Atmospheres*, *128*(12), e2022JD037700. https://doi.org/10.1029/2022jd037700

Lareau, N. P., & Clements, C. B. (2015). Cold smoke: Smoke-induced density currents cause unexpected smoke transport near large wildfires. *Atmospheric Chemistry and Physics*, *15*(20), 11513–11520. https://doi.org/10.5194/acp-15-11513-2015

Lareau, N. P., & Clements, C. B. (2017). The mean and turbulent properties of a wildfire convective plume. *Journal of Applied Meteorology and Climatology*, *56*(8), 2289–2299. https://doi.org/10.1175/jamc-d-16-0384.1

Lenschow, D. H., Wulfmeyer, V., & Senff, C. (2000). Measuring second-through fourth-order moments in noisy data. *Journal of Atmospheric and Oceanic Technology*, *17*(10), 1330–1347. https://doi.org/10.1175/1520-0426(2000)017<1330:mstfom>2.0.co;2

McClure, C. D., & Jaffe, D. A. (2018). US particulate matter air quality improves except in wildfire-prone areas. *Proceedings of the National Academy of Sciences*, *115*(31), 7901–7906. https://doi.org/10.1073/pnas.1804353115

National Interagency Fire Center. (2023). The WFIGS Interagency Fire Perimeters [Dataset]. *National Interagency Fire Center*. Retrieved from https://data-nifc.opendata.arcgis.com

NOAA Chemical Sciences Laboratory. (2022). CalFiDE measurements [Dataset]. *Chemical Sciences Laboratory*. Retrieved from https://csl.noaa.gov/groups/csl7/measurements/2022calfide/

Noyes, K. J., & Kahn, R. A. (2024). Satellite multi-angle observations of wildfire smoke plumes during the CalFiDE field campaign: Aerosol plume heights, particle property evolution, and aging timescales. *Journal of Geophysical Research: Atmospheres*, *129*(3), e2023JD039041. https://doi.org/10.1029/2023jd039041

O'Dell, K., Ford, B., Fischer, E. V., & Pierce, J. R. (2019). Contribution of wildland-fire smoke to US $PM_{2.5}$ and its influence on recent trends. *Environmental Science & Technology*, *53*(4), 1797–1804. https://doi.org/10.1021/acs.est.8b05430

Olsson, L. E., Elliott, W. P., & Hsu, S. I. (1973). Marine air penetration in western Oregon: An observational study. *Monthly Weather Review*, *101*(4), 356–362. https://doi.org/10.1175/1520-0493(1973)101<0356:mapiwo>2.3.co;2

Pahlow, M., Kleissl, J., & Parlange, M. B. (2005). Atmospheric boundary-layer structure observed during a haze event due to forest-fire smoke. *Boundary-Layer Meteorology*, *114*(1), 53–70. https://doi.org/10.1007/s10546-004-6350-z

Pan, K., & Faloona, I. C. (2022). The impacts of wildfires on ozone production and boundary layer dynamics in California's Central Valley. *Atmospheric Chemistry and Physics*, *22*(14), 9681–9702. https://doi.org/10.5194/acp-22-9681-2022

Robock, A. (1988). Enhancement of surface cooling due to forest fire moke. *Science*, *242*(4880), 911–913. https://doi.org/10.1126/science.242.4880.911

Robock, A. (1991). Surface cooling due to forest fire smoke. *Journal of Geophysical Research*, *96*(D11), 20869–20878. https://doi.org/10.1029/91jd02043

Schroeder, P., Brewer, W. A., Choukulkar, A., Weickmann, A., Zucker, M., Holloway, M. W., & Sandberg, S. (2020). A compact, flexible, and robust micropulsed Doppler lidar. *Journal of Atmospheric and Oceanic Technology*, *37*(8), 1387–1402. https://doi.org/10.1175/jtech-d-19-0142.1

Segal, M., & Arritt, R. W. (1992). Nonclassical mesoscale circulations caused by surface sensible heat-flux gradients. *Bulletin of the American Meteorological Society*, *73*(10), 1593–1604. https://doi.org/10.1175/1520-0477(1992)073<1593:nmccbs>2.0.co;2

Segal, M., Weaver, J., & Purdom, J. F. W. (1989). Some effects of the Yellowstone fire smoke plume on northeast Colorado at the end of summer 1988. *Monthly Weather Review*, *117*(10), 2278–2284. https://doi.org/10.1175/1520-0493(1989)117<2278:seotyf>2.0.co;2

Simpson, J. E., & Britter, R. E. (1980). A laboratory model of an atmospheric mesofront. *Quarterly Journal of the Royal Meteorological Society*, *106*(449), 485–500.

Stone, R. S., Augustine, J. A., Dutton, E. G., O'Neill, N. T., & Saha, A. (2011). Empirical determinations of the longwave and shortwave radiative forcing efficiencies of wildfire smoke. *Journal of Geophysical Research*, *116*(D12), D12207. https://doi.org/10.1029/2010jd015471

Strobach, E. J., Brewer, W. A., Senff, C. J., Baidar, S., & McCarty, B. (2023). Isolating and investigating updrafts induced by wildland fires using an airborne Doppler lidar during FIREX-AQ. *Journal of Geophysical Research: Atmospheres*, *128*(14), e2023JD038809. https://doi.org/10.1029/2023jd038809

Strobach, E. J., Carroll, B. J., Baidar, S., Brown, S. S., Ahmadov, R., Brewer, W. A., et al. (2024). A case study featuring the time evolution of a fire-induced plume jet over the rum creek fire: Mechanisms, processes, and dynamical interplay. *Journal of Geophysical Research: Atmospheres*, *129*(10), e2023JD040483. https://doi.org/10.1029/2023jd040483

US Environmental Protection Agency. (2024). *Air Quality System Data Mart*. [internet database]. United States Environmental Protection Agency. Retrieved from https://www.epa.gov/outdoor-air-quality-data

Wakimoto, R. M. (1982). The life cycle of thunderstorm gust fronts as viewed with Doppler radar and rawinsonde data. *Monthly Weather Review*, *110*(8), 1060–1082. https://doi.org/10.1175/1520-0493(1982)110<1060:tlcotg>2.0.co;2

Youn, D., Park, R. J., Jeong, J. I., Moon, B. K., Yeh, S. W., Kim, Y. H., et al. (2011). Impacts of aerosols on regional meteorology due to Siberian forest fires in May 2003. *Atmospheric Environment*, *45*(7), 1407–1412. https://doi.org/10.1016/j.atmosenv.2010.12.028